

WAVE BREAKING EFFECTS ON MEAN SURF ZONE HYDRODYNAMICS

Jebbe van der Werf^{1,2}, Kevin Neessen², Jan Ribberink², Wouter Kranenburg²

Abstract

In this paper we analyze the wave flume data of Boers (2005) to better understand the mean (wave-averaged) surf zone hydrodynamics. We compare the data to analytical expressions from literature and use the data to validate the phase-averaged modeling system Delft3D. Our analysis shows that the radiation stress and wave force are fairly uniformly distributed over the vertical below the wave trough level, and best predicted by the Mellor (2008) formula suggesting that part of the radiation stress under non-breaking waves is contained between the wave trough and wave crest level. The validation shows that the mean velocity profile computed by Delft3D agrees fairly well with the measured data, despite an overprediction of the turbulent kinetic energy and an underprediction of the roller force. Applying the adjusted Mellor (2008) model and a vertically-distributed instead of a surface roller force might improve the Delft3D modeling results.

Key words: laboratory experiments, modeling, surf zone hydrodynamics, turbulence, undertow, wave breaking.

1. Introduction

Wave breaking has a strong effect on surf zone hydrodynamics. Under breaking waves, the wave-driven radiation stress gradient is not uniform over the depth, but highest near the surface from where it decreases to the bed. The opposing pressure gradient due to wave set-up has a (nearly) uniform vertical distribution. This tends to result into a seaward wave-averaged current near the seabed and an onshore flow higher in the water column. This vertical undertow profile is affected by wave-breaking induced turbulence, especially near the surface, which enhances the mixing of momentum.

The undertow is important for the current-related suspended load under breaking waves. The balance between this typically offshore-directed sand transport and the typically onshore-directed bedload and wave-related suspended load determines to a large degree the cross-shore morphological evolution of natural bed features (e.g. breaker bars) and human interventions (e.g. shoreface sand nourishments).

In this paper we analyze the wave flume data of Boers (2005) to better understand mean surf zone hydrodynamics and validate analytical and numerical models. In particular, we focus on the vertical distribution of the radiation stress, wave forces, turbulence and undertow.

2. Analysis laboratory data Boers (2005)

2.1. Description experiments

Boers (2005) carried out very detailed velocity measurements in the 40 m long, 0.8 m wide and 1.05 m deep wave flume of Delft University of Technology. The uniqueness of this data set lies in the high spatial resolution, and the small measurement volume and sampling frequency such that turbulent motions were accurately measured. The fixed bed profile was based on a natural beach and included two breaker bars with a trough in between (see Figure 1). The still water level was at 0.75 above the flume bottom. In this

¹Marine & Coastal Systems, Deltares, P.O. Box 177, 2600 MH Delft, The Netherlands. E-mail address: jebbe.vanderwerf@deltares.nl

²Water Engineering & Management, P.O. Box 217, 7500 AE Enschede, University of Twente, The Netherlands. E-mail addresses: kevinneessen@gmail.com, j.s.ribberink@utwente.nl, w.m.kranenburg@utwente.nl

paper we study data from two irregular wave (JONSWAP spectrum) conditions: 1B and 1C. Table 1 shows the experimental conditions, including the surf similarity parameter ξ . Figure 1 shows the significant wave heights based on the measured spectrum and the cross-shore locations on which we focus our analyses.

Table 1. Wave conditions Boers (2005) experiments.

Case	H_{m0} (m)	T_p (s)	ξ (-)	Breaker type
1B	0.206	2.03	0.31	Spilling
1C	0.103	3.33	0.71	Weakly plunging

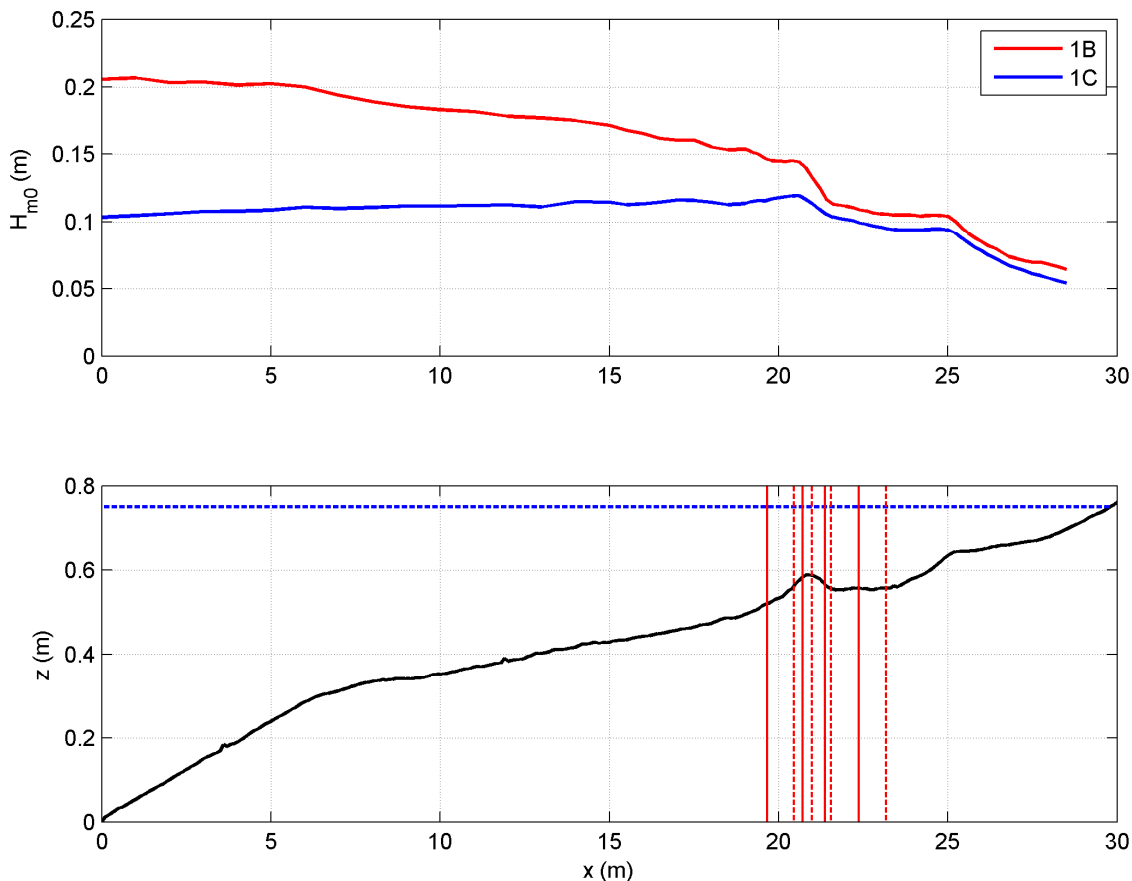


Figure 1. Measured wave heights (upper panel) and bed profile (lower panel). The dashed blue line in the lower panel represents the still water level; the red lines the measurement locations on which we focus our data analysis (solid: radiation stresses, turbulence and undertow; dashed: wave forces).

2.2. Radiation stresses

We start our analysis of conditions 1B and 1C with the computation of the radiation stress. The radiation stress is the wave-averaged horizontal flux of horizontal momentum due to the wave motion. It is usually defined in the context of the depth-integrated momentum equation (see Svendsen, 2006):

$$\rho \frac{\partial}{\partial x} \left(\int_{-h}^{\bar{\zeta}} \bar{u}^2 dz \right) + \frac{\partial S_{xx}}{\partial x} = -\rho g D \frac{\partial \bar{\zeta}}{\partial x} - \bar{v}_{b,x} \quad (1)$$

where ρ is the water density, x the horizontal direction, u the velocity in x -direction, z the vertical coordinate, $z = -h$ the bed level, $z = \bar{\zeta}$ the water surface elevation, S_{xx} the radiation stress in x -direction that

works on the plane normal to the x -direction, $D = (\bar{\zeta} + h)$ the mean water depth and $\tau_{b,x}$ the bed shear stress; the overbar denotes wave-averaging. In Eq. (1) we have omitted the mass flux term (steady situation), the convective acceleration associated with the mass flux in the wave, the surface stresses and the viscosity term. The radiation stress is defined by (see Stive & Wind, 1982):

$$\begin{aligned}
 S_{xx} &= \overline{\int_{-h}^{\zeta} (\rho \tilde{u}^2 + \rho u'^2 + p) dz} - \frac{1}{2} \rho g D^2 \\
 &= \overline{\int_{-h}^{\zeta} (\rho \tilde{u}^2 + \rho u'^2 - \rho \tilde{w}^2 - \rho w'^2) dz} - \frac{1}{2} \rho g \bar{\zeta}^2 \\
 &= \overline{\int_{-h}^{\zeta_t} (\rho \tilde{u}^2 + \rho u'^2 - \rho \tilde{w}^2 - \rho w'^2) dz} + \overline{\int_{\zeta_t}^{\zeta} (\rho \tilde{u}^2 + \rho u'^2 - \rho \tilde{w}^2 - \rho w'^2) dz} - \frac{1}{2} \rho g \bar{\zeta}^2
 \end{aligned} \tag{2}$$

with ζ_t the wave trough level, w the vertical velocity, p the pressure, and in which we have decomposed the velocities in a wave-averaged, oscillatory and turbulent component, i.e. $u = \bar{u} + \tilde{u} + u'$. Note that turbulence is not always included in formulas for radiation stress, but we do consider turbulence to be part of radiation stress following Stive & Wind (1982). Neessen (2012) showed that the contribution of the turbulence terms to radiation stress is minor in the Boers experiments, except for at the breaker bar where the turbulence contributions reach 10-30% at the mean surface level compared to the dominant $\rho \tilde{u}^2$ term.

Since the pressure due to set-up is nearly uniform over the depth (Nielsen, 1992), the depth-dependent radiation stress below the wave trough level follows from Eq. (2):

$$s_{xx,t} = \overline{\rho \tilde{u}^2} + \overline{\rho u'^2} - \overline{\rho \tilde{w}^2} - \overline{\rho w'^2} - \frac{1}{2D} \rho g \bar{\zeta}^2 \tag{3}$$

where we now use a lower case to indicate depth-dependent radiation stress in contrast with the upper case for the depth-integration radiation stress (Eq. 2)

Figure 2 shows the radiation stresses computed using Eq. (3), interpolated both along the bed profile and in the vertical direction. The figure shows that the radiation stress peaks at the two breaker bars, and that the stresses are higher for the more energetic 1B case. The radiation stress appears to be fairly uniformly distributed over the water depth, except for case 1B at the most offshore-located breaker bar.

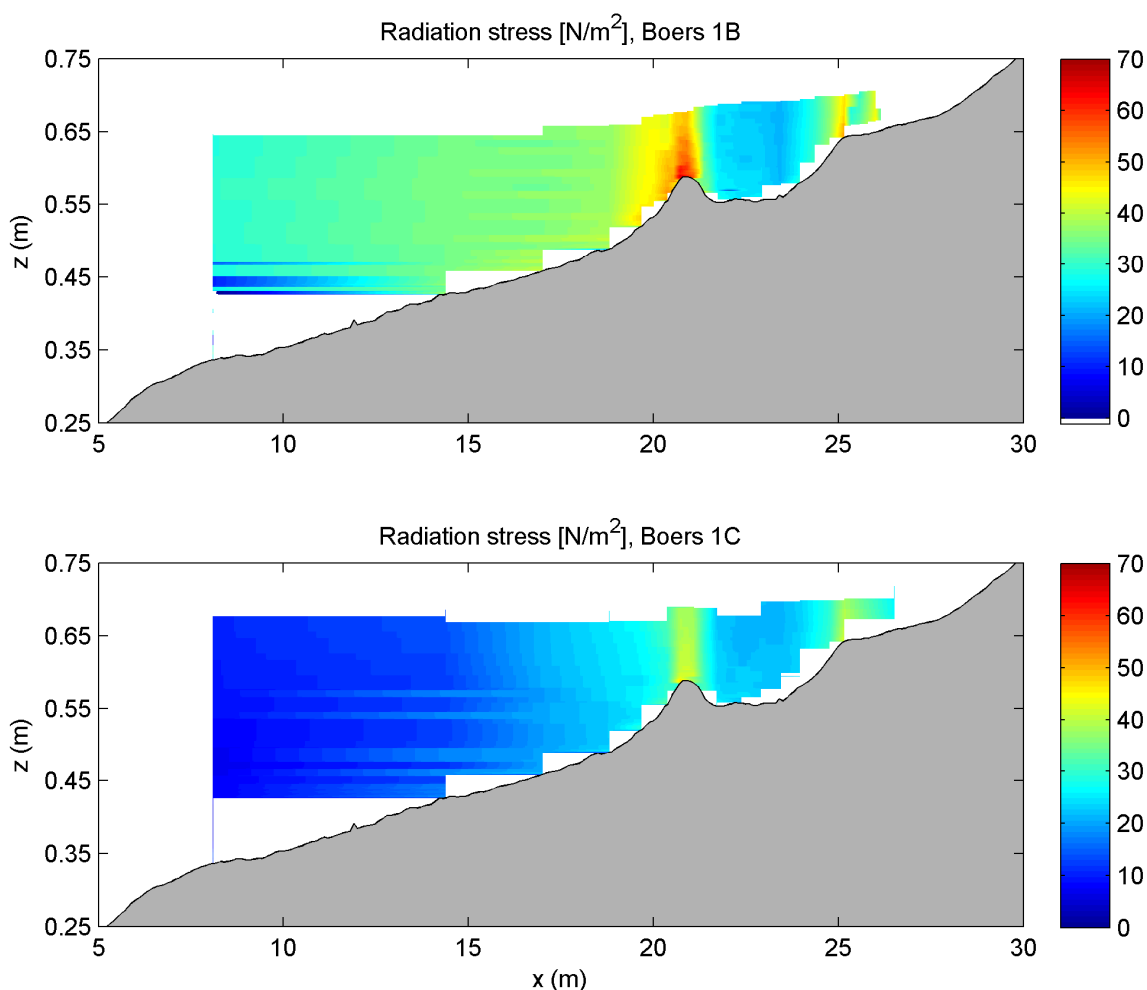


Figure 2. Radiation stress based on measured velocities for Boers cases 1B (upper panel) and 1C (lower panel).

Next, we compare the radiation stress as computed from the measured velocities with expressions from literature. Based on linear wave theory and assuming small wave amplitude, Longuet-Higgins & Stewart (1964) (LHS64) derived the following expression for the depth-integrated radiation stress:

$$S_{xx} = (2n - 0.5)E \quad (3)$$

for normal incident waves and with E the wave energy, $n = c_g/c$, c_g the wave group celerity and c the wave phase celerity. More recently, Mellor (2008) (M08) propose for the depth-dependent radiation stress:

$$s_{xx} = kE (F_{cs}F_{cc} - F_{sc}F_{ss}) + F_{ed}E_d \quad (4)$$

with F_{cs} , F_{cc} , F_{sc} , F_{ss} shape functions depending on water depth and wave number k . This expression is based on linear wave theory too. E_d represents the radiation stress between wave crest and wave trough and equals $0.5 \cdot E$ such that depth-integrated radiation stress equals the LHS64 expression. Mellor applied E_d at the mean water surface. However, here we follow Kumar et al. (2011) and vertically distribute with the F_{ed} function:

$$F_{ed} = \frac{FB}{\int_{-h}^{\zeta} FB dz}$$

$$FB = \cosh \left[\frac{2\pi}{H_{rms}} (z + h) \right] \quad (5)$$

with a length that scales with the root-mean-square wave height H_{rms} . Kumar et al. showed that this updated vertical distribution reduced significantly the spurious flows that were created when implementing the original M08 radiation stress forcing in Regional Ocean Modeling System (ROMS).

As discussed by e.g. Boers (2005) the breaking-induced roller between the wave crest and trough also induces a mean horizontal momentum flux with a depth-integrated value of $2 * E_r$ with E_r the wave roller energy. The latter is estimated by Boers (2005) based on the wave roller mass flux that follows from the measured wave-averaged velocities, the computed wave mass flux (Stokes drift) and the measured wave phase celerity. In line with Kumar et al. (2011) we will distribute the roller contribution vertically using Eq. (5).

It should be noted that both the LHS64 and M08 models do not include the effect of turbulence. Although the contribution of turbulence to radiation stress is in general minor (as discussed above), this could explain differences between observations and computations, especially near the water surface at the breaker bar.

Figures 4 and 5 compare measured and computed depth-dependent radiation stresses at four cross-shore locations with

$$\sigma = \frac{z - \bar{\zeta}}{D} \quad (6)$$

the dimensionless vertical level. The LHS64 radiation stress is made “depth-dependent” by dividing it by the water depth.

These figures show that measured radiation stresses are quite uniformly distributed over the water column, except inside the wave boundary layer. The stresses are best reproduced by the M08 formula. Unfortunately, we have no data to verify the presence and vertical distribution of the E_d and roller contributions, as we discarded the measurement data above the wave trough since these were unreliable. Further comparison shows that the LHS64 expression overpredicts radiation stresses in all cases, supporting the presence of a stress between wave trough and crest for non-breaking waves. The radiation stresses are well predicted by the M08 formula for the 1B case and slightly overpredicted for the 1C case. According to the predictions, the roller contribution becomes increasingly important when approaching the shore.

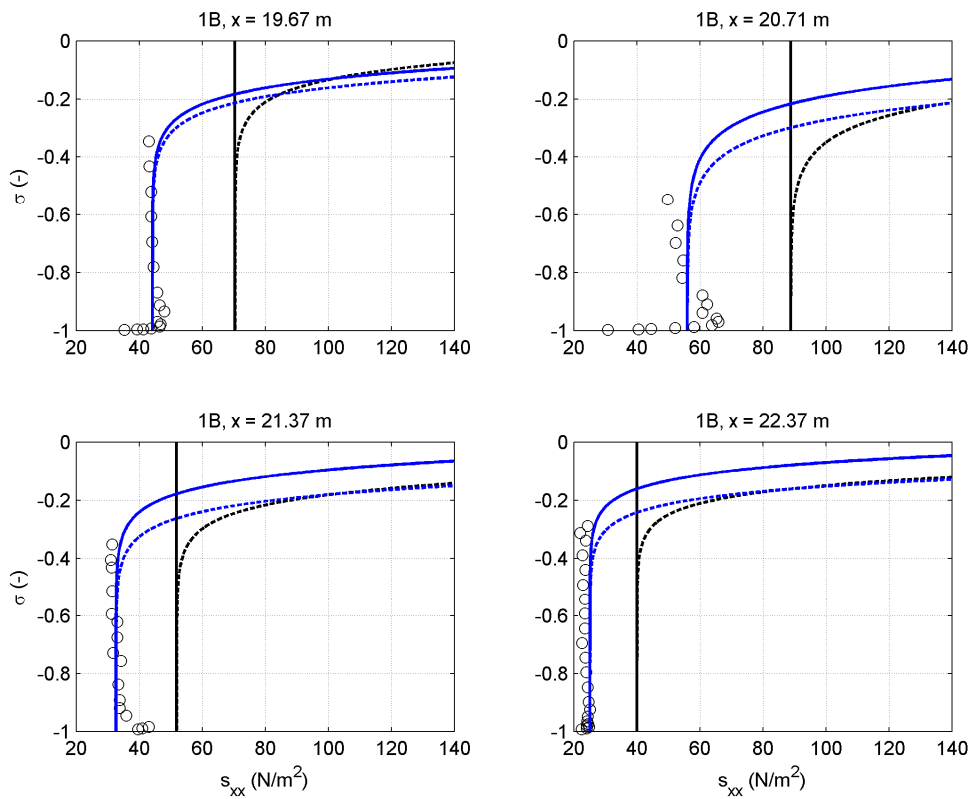


Figure 3. Depth-dependent radiation stresses at four cross-shore locations for case 1B. Circles: measured, black solid lines: LHS64, black dashed lines: LHS64 + roller, blue solid lines: M08, blue dashed lines: M08 + roller.

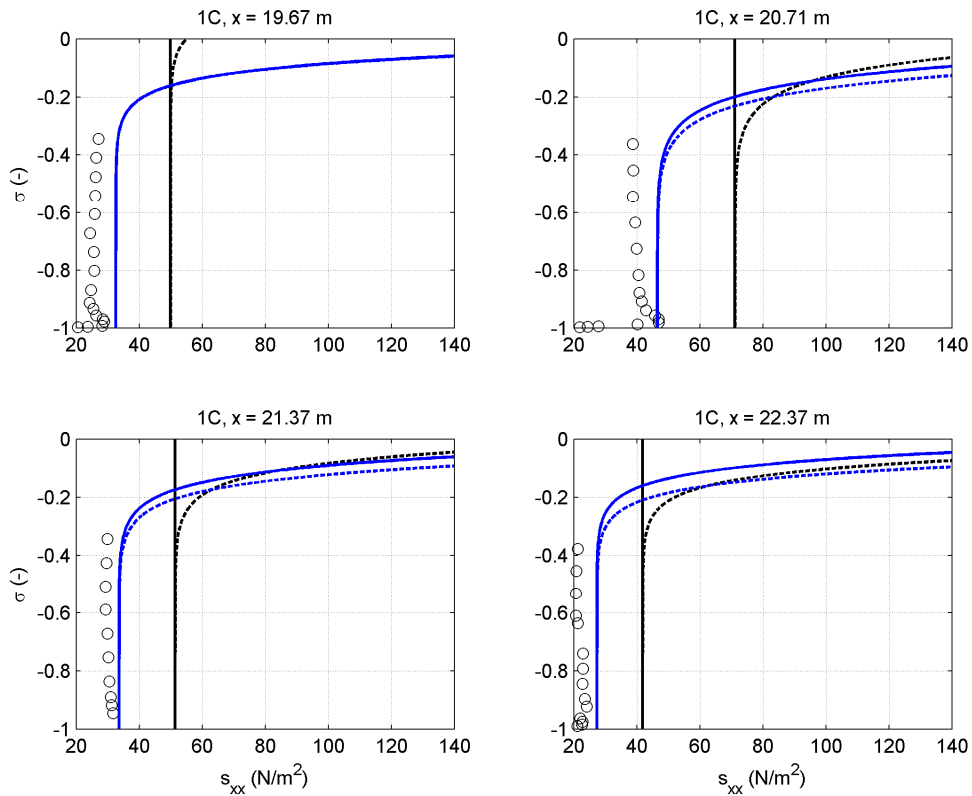


Figure 4. Depth-dependent radiation stresses at four cross-shore locations for case 1C. Circles: measured, black solid lines: LHS64, black dashed lines: LHS64 + roller, blue solid lines: M08, blue dashed lines: M08 + roller.

2.3. Wave forces

Next we study the horizontal radiation stress gradient; the wave force that actually affects the mean flow:

$$f_{xx} = -\frac{\partial s_{xx}}{\partial x} \quad (7)$$

Note that we use a lower case to indicate depth-dependent wave force. We only consider the area around the breaker bar where measurement density was highest such that reliable wave forces could be determined. This is also the location where wave forces are highest. The interpolated radiation stress field (Figure 2) was used as basis to compute the wave forces. The derived wave force is assigned to the horizontal position in between two measurement locations (Figure 1). Figure 5 show the resulting wave force. Figures 6 and 7 compare the measured and computed wave forces at four cross-shore locations.

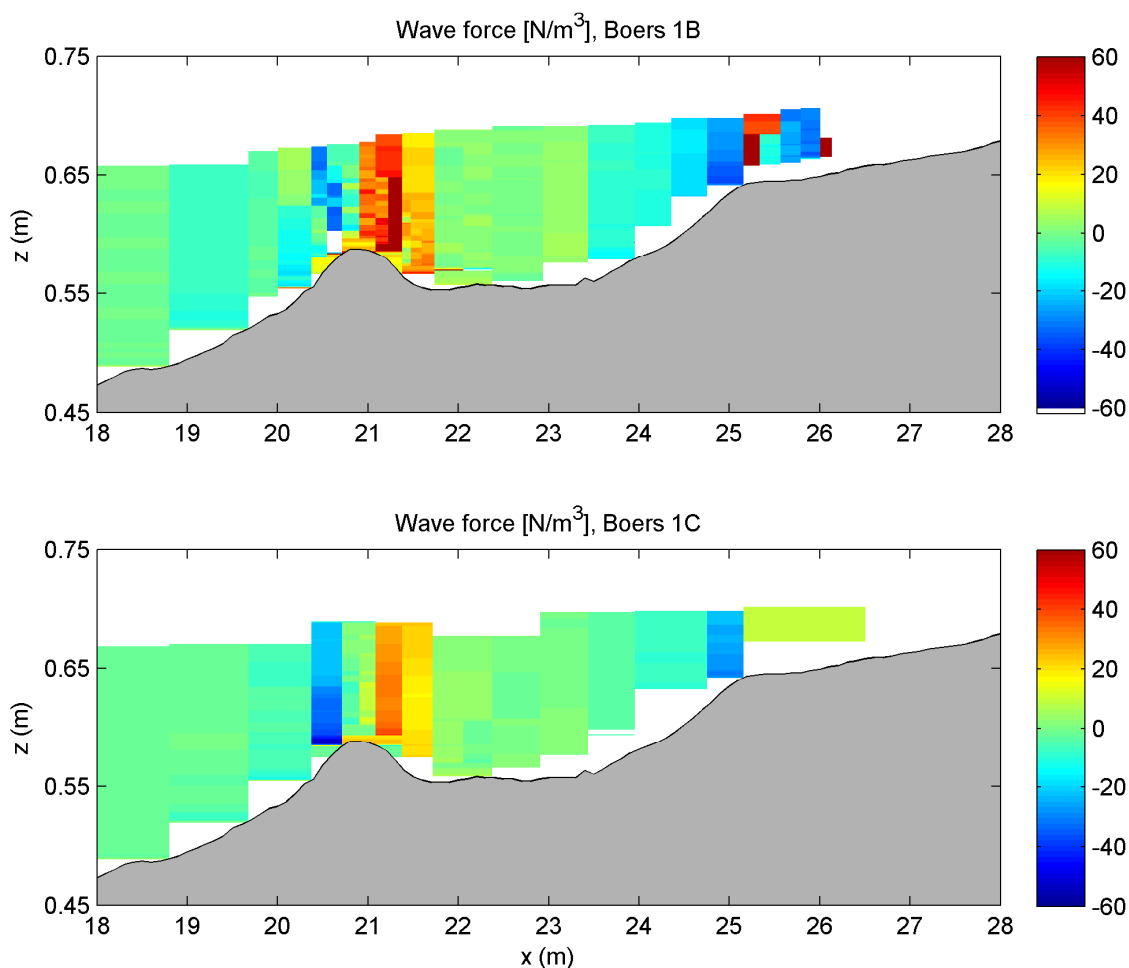


Figure 5. Wave forces based on measured velocities for Boers cases 1B (upper panel) and 1C (lower panel).

Figure 5 shows that wave forces are negative (i.e. offshore-directed) at the offshore flanks of the breaker bars. As Eq. (1) shows, this is (mainly) compensated by onshore-directed pressure force as the advective and bed shear stress term are generally small (Svendsen, 2006). This means the pressure gradient is negative and thus set down occurs, in line with theory and the water level measurements of Boers (2005). At around $x = 20.7$ m (just before the crest of the breaker bar), the wave forces switch sign and become positive, leading to setup in accordance with the measured water levels. The maximum wave forces occur around $x = 21.3$ m, after which wave forces decrease in magnitude in through between the breaker bars.

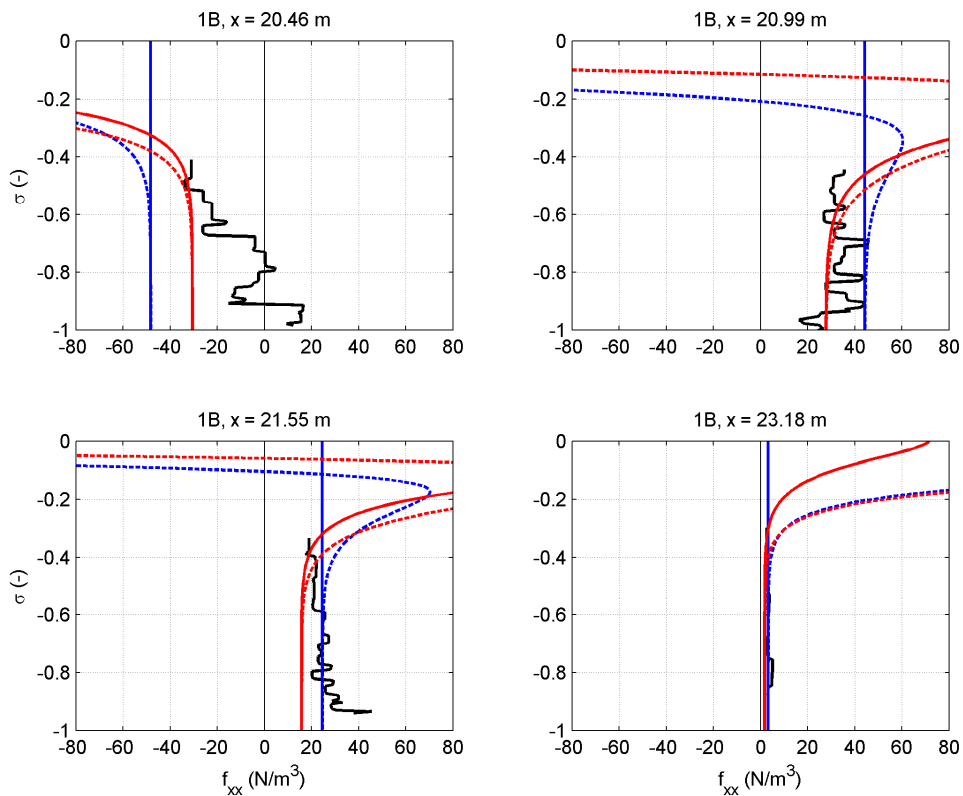


Figure 6. Depth-dependent wave forces at four cross-shore locations for case 1B. Black lines: measured, blue solid lines: LHS64, blue dashed lines: LHS64 + roller, red solid lines: M08, red dashed lines: M08 + roller.

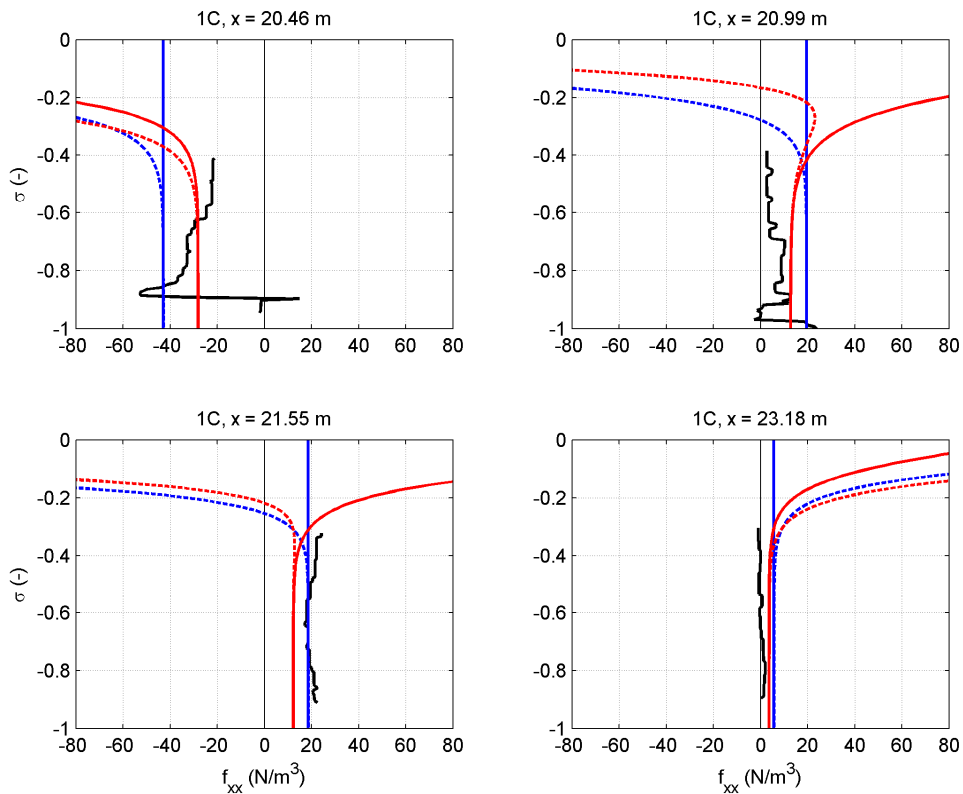


Figure 7. Depth-dependent wave forces at four cross-shore locations for case 1C. Black lines: measured, blue solid lines: LHS64, blue dashed lines: LHS64 + roller, red solid lines: M08, red dashed lines: M08 + roller.

Figures 6 and 7 also show the wave forces as computed from the M08 and LHS64 formulas. The figures show that the difference between these two expressions is not as large as for the radiations stresses, which is due to the fact that wave force results from the horizontal gradient of the radiations stress. However, the agreement with the measured data is still best for the M08 method. Both methods reproduce the offshore-directed (negative) wave force at $x = 20.46$ m, followed by onshore-directed (positive) wave forces at the three more onshore locations. Including the roller contribution gives higher negative wave forces at the most offshore location (as roller energy is increasing) and higher positive wave at the most onshore location (as roller energy is decreasing). In between we see that the roller contribution changes sign in the vertical direction, which is mainly related to the shape function according to Eq. (5) with vertical scale related to the wave height. Furthermore, it appears that the models perform worst close to the bed, which could be of significance for sand transport, as sand concentrations are highest near the bed.

3. Delft3D modeling

3.1 Delft3D model set-up

Finally, we compare the data of Boers to computations with the numerical model Delft3D. Delft3D is a phase-averaged 3D modeling system solving coupled equations for waves, currents, sediment transport and bed level evolution (Lesser et al, 2004). The wave module supplies the wave forces, which contain a roller contribution imposed at the water surface:

$$F_{x,r} = \frac{D_r}{c} \quad (8)$$

and a depth-invariant part:

$$F_{x,w} = -\frac{\partial S_{xx}}{\partial x} - F_{x,r} \quad (9)$$

with

$$S_{xx} = (2n - 0.5)E + 2E_r \quad (10)$$

and where D_r the dissipation of roller energy. This is similar to Eqs. (4) and (7) with the main difference that the roller force is by definition positive in Delft3D and applied at the surface only. The depth-invariant wave force is mainly balanced by the pressure gradient (water level set-down and set-up), whereas the roller force drives an onshore mean velocity in the upper part of the water column resulting in an offshore mean velocity in the lower part of the water column (the so-called undertow).

The turbulence model includes source terms in both the equations for turbulent kinetic energy and turbulent kinetic energy dissipation to account for wave breaking and bed friction in the wave boundary layer. The contribution due to wave breaking is linearly distributed over half a wave height below the mean water surface (Walstra et al., 2000). The (Eulerian) current velocities include offshore return currents compensating for the onshore-directed Stokes (M_s) and roller mass flux (M_r), with $M_s = E/c$ and $M_r = 2*E_r/c$ based on linear wave theory.

We have set up a 2DV Delft3D model to simulate the Boers cases with a 0.2 m grid resolution in the horizontal direction and 15 σ -layers with the highest resolution near the water surface and the bed. The time step was 0.6 s. Standard model settings were used. More information on the model set-up can be found in Neessen (2012).

Delft3D was calibrated against the measured wave heights and mean water levels, separately for Case 1B and 1C. The top panel of Figure 8 shows that in general the measured wave heights are well reproduced by Delft3D. Some differences occur for the 1B case: the modeled energy dissipation between $x \approx 4$ and 14 m and near the breaker bar ($x \approx 21$ -22 m) is too low leading to a slight wave height overprediction.

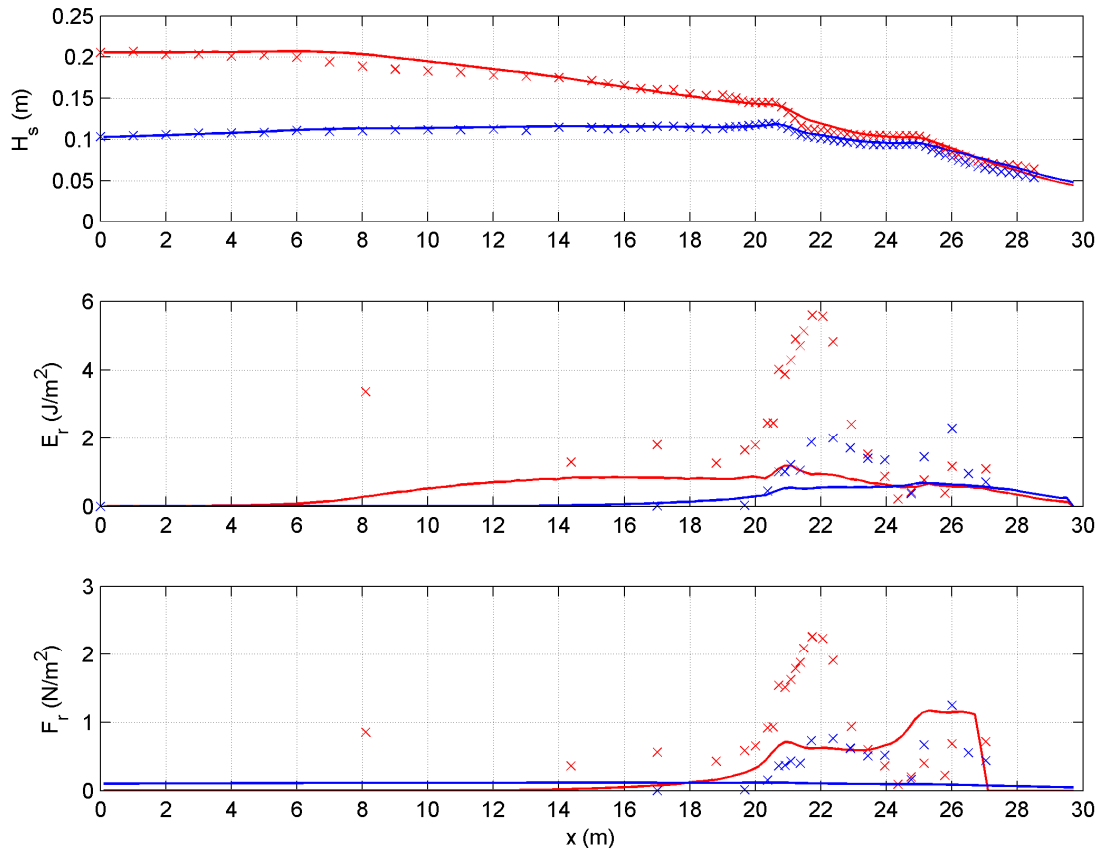


Figure 8. Comparison between measured (crosses) and Delft3D simulated (solid lines) wave heights (upper panel), roller energy (middle panel) and roller force (lower panel) for 1B (red crosses, lines) and 1C (blue crosses and lines).

The figure also show the roller force according to Eq. (8) with $D_r = 2K_l g E_r / c^2$ ($K_l = 0.044$) fitted by Boers (2005) to the turbulent shear stress at the mean water level that followed from a linear extrapolation of the measured turbulent stresses. These will be discussed in the next section.

3.2 Turbulent kinetic energy and mean current

Figure 9 compares measured and predicted vertical profiles of the mean turbulent kinetic energy (*tke*). This figure shows that Delft3D tends to overpredict *tke* for both cases, especially at the two locations before the first breaker bar ($x = 19.7$ and 20.7 m). The agreement is somewhat better at the two locations onshore of the breaker bar ($x = 21.4$ and 22.4 m). The increased *tke* in the wave boundary layer (both the magnitude and the vertical extent) computed by Delft3D is not very apparent in the measured values.

Figure 10 compares measured and computed profiles of the mean (wave-averaged) current. At all four locations the mean current profile is offshore-directed due to the return flow (undertow) compensating for the onshore mass flux between the wave trough and wave crest. Delft3D tends to overpredict the undertow, except for the two locations onshore from the breaker bar ($x = 21.4$ and 22.4 m) where the agreement is good for Case 1B. The overprediction points to an overprediction of the mass flux, which could be attributed to the wave height overprediction as shown in Figure 8 (mainly the 1B case). The measured curvature in the mean current profiles is larger than computed. This is mainly due to the underprediction of roller forces (Figure 8) and an overprediction of the *tke* (Figure 9) at the considered locations.

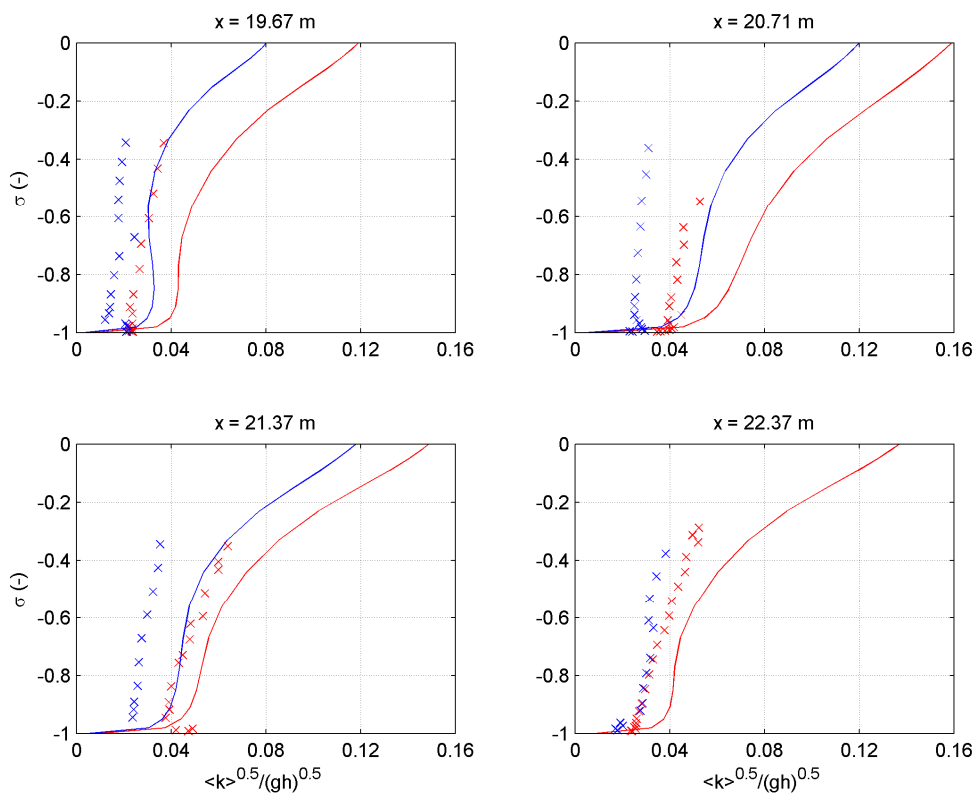


Figure 9. Comparison against measured (crosses) and simulated (solid lines) vertical profiles of the mean turbulent kinetic energy at four cross-shore locations for Case 1B (red crosses and lines) and 1C (blue crosses and lines).

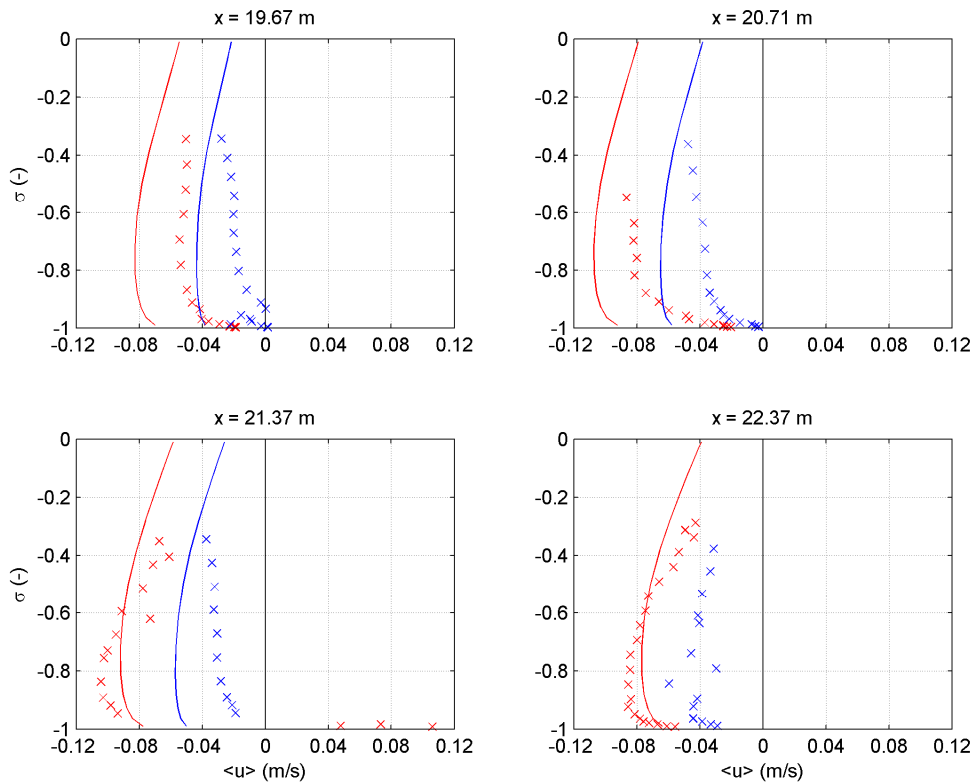


Figure 10. Comparison against measured (crosses) and simulated (solid lines) vertical profiles of the mean current at four cross-shore locations for Case 1B (red crosses and lines) and 1C (blue crosses and lines).

4. Conclusions and recommendations

The main conclusions from the analysis of the wave flume data of Boers (2005), and the comparison between this data-set and analytical expressions and Delft3D are:

1. Below the wave trough level, the radiation stress and the associated wave forces are fairly uniformly distributed over the water column.
2. The formula of Mellor (2008) better reproduces measured depth-dependent radiation stresses and wave forces below the wave trough level than the depth-integrated Longuet-Higgins (1964) approach, suggesting that part of the radiation stress under non-breaking waves takes place in between the wave crest and wave trough. Largest deviations occur in the lower part in the water column, which could be of great importance for sand transport, as sand concentrations are highest near the bed.
3. The Delft3D model generally overpredicts the turbulent kinetic energy and underpredicts the roller forces, resulting in an underprediction of the curvature of the mean current profile. Despite, it reproduces the measured mean current profiles fairly well. Agreement between measurements and observations is best onshore from the first breaker bar.

Based on this, we recommend testing the Mellor (2008) model as adjusted by Kumar et al (2011) for the vertical distribution of the radiation stress and a vertically-distributed instead of a surface roller force within Delft3D, as this might improve the computed mean velocity profiles. Furthermore, we recommend investigating how the vertical gradient of the mean horizontal velocity depends on the (vertical distribution of) wave forces, turbulent viscosity, pressure and bed shear stress to better understand the physical processes driving the undertow, and to assess which model components need further improvement.

Acknowledgements

Marien Boers from Deltares is acknowledged for sharing his laboratory data. The research is partly carried out in the framework of the Dutch/UK collaboration research project SINBAD, jointly funded by STW (grant 12058 for the Dutch part) and EPSRC (grant EP/J00507X/1 for the UK part), and partly in the framework of the Deltares strategic research program Coastal Morphodynamics (project number 120.2359).

References

- Boers, M., 2005. Surf zone turbulence. Ph.D. thesis, Delft University of Technology, The Netherlands.
- Kumar, N., Voulgaris, G., Warner, J.C., 2011. Implementation and modification of a three-dimensional radiation stress formulation for surf zone and rip-current applications. *Coastal Engineering*, 58: 1097-1117.
- Lesser, G.R., Roelvink, J.A., Van Kester, J.A.T.M., Stelling, G.S., 2004. Development and validation of a three dimensional morphological model. *Coastal Engineering*, 51: 883-915.
- Longuet-Higgins, M.S., Stewart, R.W., 1964. Radiation stresses in water waves: a physical discussion, with applications. *Deep-sea Research*, 11: 529-562
- Mellor, G.L., 2008. The depth-dependent current and wave interaction equations: a revision. *Journal of Physical Oceanography*, 38: 2587-2596.
- Neessen, K.C.C.J., 2012. Analysing depth-dependence of cross-shore mean-flow in the surf zone. M.Sc. thesis, University of Twente, The Netherlands.
- Nielsen, P., 1992. Coastal bottom boundary layers and sediment transport. *Advanced Series on Ocean Engineering*, Volume 4, World Scientific Publishing, Singapore.
- Stive, M.J.F., Wind, H.G., 1982. A study of radiation stress and set-up in the nearshore region. *Coastal Engineering*, 6: 1-25.
- Svendsen, I.A., 2006. Introduction to nearshore hydrodynamics. *Advanced Series on Ocean Engineering*, Volume 24, World Scientific Publishing, Singapore.
- Walstra, D.J.R., Roelvink, J.A., Groeneweg, J., 2000. Calculation of Wave-Driven Currents in a 3D Mean Flow Model. *Proceedings 27th ICCE*, Sydney, Australia.